nature photonics

LETTERS

https://doi.org/10.1038/s41566-020-0644-7

Check for updates

Strong mid-infrared photoresponse in small-twist-angle bilayer graphene

Bingchen Deng[1,4], Chao Ma[1,4], Qiyue Wang[2,4], Shaofan Yuan[1,4], Kenji Watanabe[3], Takashi Taniguchi[3], Fan Zhang[2]✉ and Fengnian Xia[1]✉

Small-twist-angle (<2°) bilayer graphene has received extraordinary attention recently due to its exciting physical properties[1–11]. Compared with monolayer graphene, the Brillouin zone folding in twisted bilayer graphene (TBG) leads to the formation of a superlattice bandgap and substantial modification to the density of states[4,6,7,12,13]. However, these emerging properties have rarely been leveraged to realize new optoelectronic devices. Here, we demonstrate the strong, gate-tunable photoresponse in the mid-infrared wavelength range of 5 to 12 μm. A maximum extrinsic photoresponsivity of 26 mA W^{-1} has been achieved at 12 μm when the Fermi level in 1.81° TBG was tuned to its superlattice bandgap. Moreover, the strong photoresponse critically depends on the formation of a superlattice bandgap, and it vanishes in the gapless case with an ultrasmall twist angle (<0.5°). Our demonstration reveals the promising optical properties of TBG and provides an alternative material platform for tunable mid-infrared optoelectronics.

Various twisted bilayer structures have recently been explored extensively as they feature many novel physical phenomena such as superconductivity and emerging topological properties[6–19]. Among these twisted bilayer systems, small-twist-angle bilayer graphene represents a particularly interesting material system. First, the emergence of a moiré pattern in TBG leads to the formation of a mini-Brillouin zone and considerably enhanced dynamical conductivity in the low-energy range[20–22]. Second, the periodic modulation of the interlayer potential in a moiré superlattice can induce bandgaps in both the electron and hole branches[4,12,13]. Third, as the two constituent graphene layers have exactly the same crystalline structure, TBG exhibits interesting physical properties even when the twist angle is large[23,24]. This phenomenon is different in graphene/hexagonal boron nitride (hBN) heterostructures, in which the heterostructure properties are strongly modified from those of the constituent layers when the crystalline directions of both layers are aligned[25–27]. However, previous light–matter interaction experiments in TBG focused on cases with relatively large twist angles using the visible or near-infrared photons[24,28–32], and in these demonstrations van Hove singularity-like electronic resonances were leveraged for enhanced light–matter interactions[23,24,28–32]. In this work, we report strong broadband mid-infrared photoresponse in small-twist-angle TBG. Furthermore, we clarify its bolometric origin through transport studies and reveal the importance of the superlattice bandgap in photoresponse.

Figure 1a shows the schematic of the TBG transistor used for mid-infrared photodetection in this work. The active channel consists of a hBN/TBG/hBN heterostructure, which is assembled using the dry transfer approach reported in refs. [4,33]. A silicon back gate is used to control the Fermi level in TBG. We present information on the detailed fabrication process in the Methods. We characterized the transport properties of the TBG transistor before performing the photocurrent measurements. Figure 1b plots the transistor source–drain resistance as a function of the back-gate bias (V_{BG}) measured at 83 K, with a source–drain bias (V_{DS}) of 10 mV. The thicknesses of the top and bottom hBN layers in this device are 30 nm and 25 nm, respectively, and its optical micrograph is shown in the inset of Fig. 1c. Resistance maxima are observed at $V_{BG} \approx \pm 43.5$ V and at ~0 V. The resistance maximum at $V_{BG} \approx 0$ V (charge-neutrality point) is due to the presence of a Dirac point in TBG[4,5,34]. The gate voltage at which charge-neutrality occurs (V_{CNP}) is always within ±2 V V_{BG} for all of the devices in this work and is subtracted from V_{BG} in the bottom x-axis in Fig. 1b,c. The resistance peaks at ±43.5 V are due to the formation of the superlattice bandgap above and below the lowest moiré Dirac bands, as illustrated in the calculated band structure in the inset of Fig. 1b (refs. [4,34]). When the Fermi level is tuned to the centre of the superlattice bandgap, the carrier density in the channel is minimized, leading to the observed resistance peaks. As reported previously[4,34], four electrons per moiré unit cell ($4n_0$) are required to fill/vacate the lowest moiré Dirac bands. We can therefore index the electron filling number in the top x-axis in Fig. 1b and infer the unit cell area (and thus the twist angle) of the device from the transport properties. Taking into account the thicknesses of the gate dielectric layers (25 nm hBN and 90 nm SiO_2), we calculate that the superlattice gaps are located at $n_{s\pm} = \pm 7.62 \times 10^{12}\,\mathrm{cm}^{-2}$ and that the superlattice unit cell area $(A) = 4/n_{s+} = 52.5\,\mathrm{nm}^2$. As $A = \frac{\sqrt{3}}{2}\left(\frac{a}{2\sin\frac{\theta}{2}}\right)^2$ and the graphene lattice constant $(a) = 0.246$ nm, a twist angle θ of 1.81° is obtained.

After characterizing the gate-dependent resistance of the TBG device, we measured the gate-dependent photocurrent at 5.0, 7.7 and 12 μm. We kept the source–drain bias at 200 mV and swept the V_{BG} in these measurements. The photocurrent was determined by comparing the source–drain current (I_{DS}) with and without light illumination on the basis of a lock-in scheme (see the Methods for detailed information on photocurrent measurements). As shown in Fig. 1c, the photocurrent results show almost identical gate-dependent trends at all three wavelengths. Moreover, there are a few salient features in the photoresponse. First, a strong photoresponse is observed when the device Fermi level is within the superlattice bandgap. At 12 μm, the extrinsic responsivity (R_{ex}) reaches

[1]Department of Electrical Engineering, Yale University, New Haven, CT, USA. [2]Department of Physics, The University of Texas at Dallas, Richardson, TX, USA. [3]National Institute for Materials Science, Tsukuba, Japan. [4]These authors contributed equally: Bingchen Deng, Chao Ma, Qiyue Wang, Shaofan Yuan. ✉e-mail: zhang@utdallas.edu; fengnian.xia@yale.edu

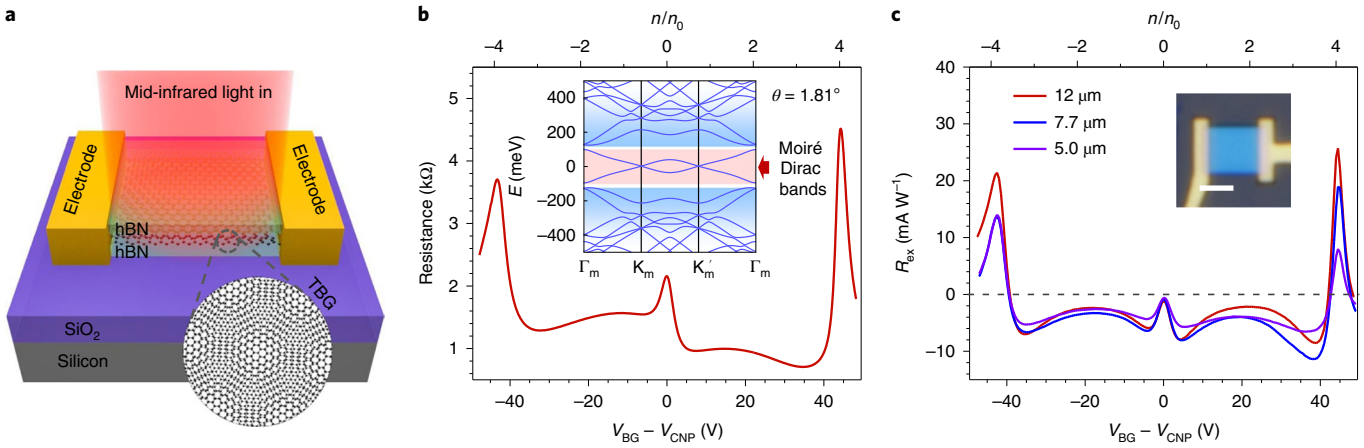

Fig. 1 | Strong mid-infrared photoresponse in 1.81° TBG. a, The schematic of the hBN-encapsulated TBG device and the photocurrent measurement scheme. **b**, The device source–drain resistance as a function of back-gate voltage at 83 K. The upper *x*-axis shows the electron filling states. The inset shows the calculated band structure of the 1.81° TBG. Two superlattice-induced bandgaps above and below the lowest moiré Dirac bands are shown. Γ_m, K_m and K'_m are high-symmetry points in the mini-Brillouin zone. **c**, The infrared photoresponse of the device at 5.0 μm, 7.7 μm and 12 μm light illumination. The extrinsic responsivity is featured by two positive peaks at both the hole- and electron-side bandgaps. Other than at (and around) the bandgap positions, the responsivity is negative. For consistency, all of the curves are horizontally shifted by their respective V_{CNP}. The V_{CNP} is within ±2 V in all of our devices. The measurements were performed at 83 K. The inset shows the optical image of the 1.81° TBG device. Scale bar, 2 μm.

26 mA W^{-1}, which is strikingly large as the channel comprises only two layers of carbon atoms. In fact, such an extrinsic responsivity is comparable to some of the early quantum-well infrared photodetectors that leverage intersubband transitions in the mid-infrared range[35,36]. However, those quantum-well infrared photodetectors usually comprise tens of pairs of quantum-well structures. Second, the photocurrent exhibits both polarities, which indicates that the channel can be both more and less conductive under light illumination, depending on the position of the gate-controlled channel Fermi level. When the Fermi level is tuned to the centre of a superlattice bandgap, a strong positive photocurrent is observed; however, the photocurrent turns negative quickly when the Fermi level deviates from the superlattice bandgap. Third, the shapes of resistance in Fig. 1b and R_{ex} in Fig. 1c are very similar, except that the photocurrent has both polarities whereas the source–drain resistance cannot be negative. In addition, there is electron-hole asymmetry in both the resistance and photocurrent measurements (Fig. 1b,c) due to the intrinsic asymmetry in the band structures. Although there are superlattice-induced bandgaps in both the electron and hole branches, the magnitudes of the bandgaps and the detailed band structures are different. Several previous experimental works suggest that the bandgap in the electron side (~60 meV) is slightly larger than that in the hole side (~50 meV) for a TBG with a twist angle of around 1.8° (refs. [7,34,37]). As we will elucidate later, the photoresponse depends on the magnitude of the bandgaps and the detailed band structures. As a result, it is not surprising to observe the asymmetry in the transport and photoresponse characteristics for all three wavelengths.

We performed TBG optical absorption calculations to clarify the origin of the photoresponse and its gate dependence. In Fig. 2a, we plot the calculated real part (Re) of TBG dynamical conductivity, $\sigma(\omega)$ (normalized to monolayer graphene conductivity, σ_0), at a twist angle of 1.81° when the Fermi level of the TBG is tuned to the middle of the superlattice bandgap on the electron side. We only consider the conductivity due to direct interband transitions in the calculation (see the Methods for more details). In the inset of Fig. 2a, we plot some possible interband transition pathways for photons at 5.0, 7.7 and 12 μm. In these transitions, the mid-infrared photons excite the electrons from the filled moiré bands to the empty moiré bands above. As shown in Fig. 2a, the dynamical conductivity right beyond the bandgap energy is about $8\sigma_0$, indicating a very strong light absorption well exceeds 4.6%, which is the absorption of light in two layers of graphene through interband transitions[38]. Although the conductivity becomes smaller at high energy range, it is still larger than $2\sigma_0$ across a broad energy range from 25 to 80 meV. The enhancement of the conductivity is due to the enhanced density of states (DOS) close to the top of the moiré Dirac bands and the bottom of the empty bands. In addition, there are also multiple energy ranges in which the conductivity is beyond $2\sigma_0$. This feature is a consequence of the presence of optical transitions between multiple pairs of moiré bands. Here we want to stress that the calculated dynamical conductivity should not be used in direct comparison with the relative photoresponse at different excitation wavelengths, due to the well-known discrepancy between experimentally measured and theoretically calculated superlattice bandgap values[4,6,7,34,37,39]. The calculated superlattice bandgap is usually around less than half of the experimental value. Taking this factor into account, at 12 μm (~100 meV), the conductivity is most likely greater than $2\sigma_0$, which explains the strong photoresponse at this wavelength.

Strong absorption of light does not directly give rise to a strong photocurrent. In our devices, the photocurrent can arise from either the intrinsic photoconductive effect or the bolometric effect. The former is due to the extra photocarriers induced by light, which make the material more conductive and hence the photocurrent is positive, whereas the latter is is a result of the change in temperature induced by light. The bolometric effect can lead to both positive and negative photocurrents, depending on the material properties. In metals and superconductors, the bolometric effect usually results in a negative photocurrent, as enhancement of temperature leads to larger resistance[40,41]. In intrinsic semiconductors, higher temperature can lead to reduced resistance due to thermal excitation of carriers[41]. We performed temperature-dependent transport characterizations and the results are plotted in Fig. 2b. The measurements were performed on a different 1.81° TBG device of the same size (3 μm × 3 μm) and made from the same hBN/TBG/hBN stack (~20 μm × 20 μm) as the one presented above. When the Fermi level is close to the electron (hole) superlattice bandgap,

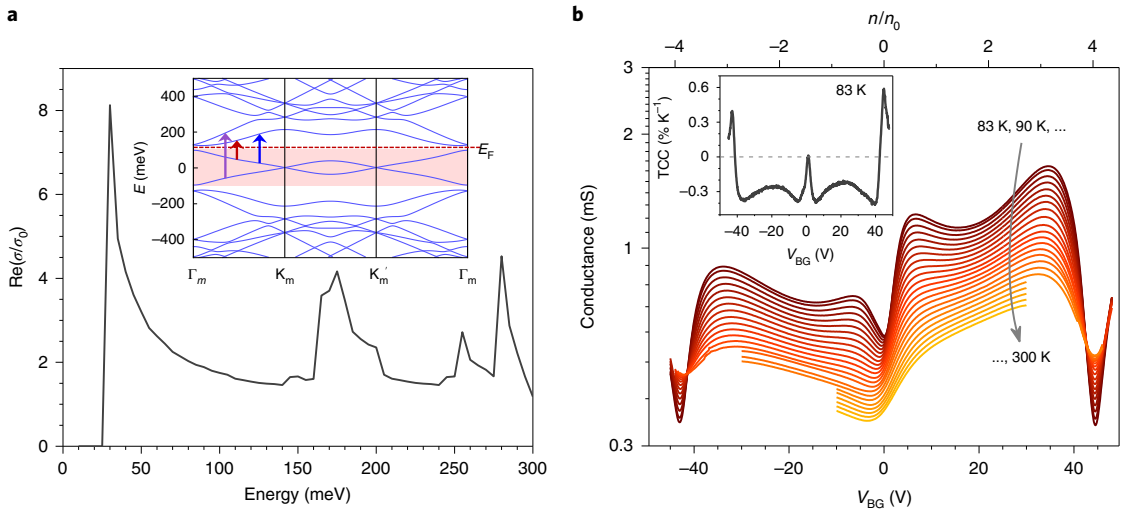

Fig. 2 | Bolometric photocurrent enhanced by moiré superlattice. a, The calculated dynamical conductivity (real part) spectrum of the 1.81° TBG when the Fermi level (E_F) is tuned to the middle of the superlattice bandgap in the electron branch. The purple, blue and red arrows in the inset indicate some possible interband transitions at 5.0 μm, 7.7 μm and 12 μm light illumination, respectively. **b**, The temperature-dependent conductance of the 1.81° TBG; the temperature ranges from 83 K to 300 K. The device shows thermal excited behaviour at V_{BG} values of around ±43.5 V, indicating the formations of superlattice-induced bandgaps. The V_{BG} scanning range is intentionally reduced at higher temperatures to keep a minimal gate leakage current. The inset shows the calculated TCC at 83 K, which is derived from the temperature-dependent conductance. The TCC has similar features to the photocurrent patterns.

which corresponds to a V_{BG} of 43.5 V (−43.5 V), the channel resistance exhibits clear semiconducting behaviour and the resistance reduces at a higher temperature. By contrast, at all other gate biases the TBG resistance increases as the temperature rises, which is a typical metallic property. In the inset of Fig. 2b, we plot the temperature coefficient of the conductance ($TCC = \frac{1}{G} \times \frac{\Delta G}{\Delta T}$, where G is the device conductance and T is temperature) measured at 83 K. The gate dependence of the TCC clearly resembles that of the photoresponse in Fig. 1c, indicating the bolometric nature of the observed photoresponse in TBG.

We also measured the photocurrent as a function of V_{DS} to further investigate the origin of the photocurrent generation and the reproducibility. As shown in Supplementary Fig. 1c, the photocurrent increases initially as V_{DS} increases and then starts to decrease at V_{DS} of ~0.1 V. This is typical for a bolometric device, as the current heats up the device and reduces the bolometric photoresponse[42]. By contrast, for a photoconductive detector, the photocurrent can saturate as the bias increases due to the carrier velocity saturation. The photoresponse starts to decrease in our device at a biasing field of around 0.03 V μm^{-1} (0.1 V source–drain bias in 3-μm-long device), as shown in Supplementary Fig. 1c. Such a decrease cannot be due to the carrier velocity saturation as the drain current does not decrease with a biasing field up to 0.17 V μm^{-1} (corresponding to V_{DS} of 0.5 V in this 3-μm-long device; see the transport measurements shown in Supplementary Fig. 1d). As a result, this observation of photoresponse reduction at a small source–drain biasing field further confirms the origin of the bolometric effect. Aside from these observations, we present frequency- and power-dependent photocurrent measurements for our TBG devices in Supplementary Section 2, in which the photocurrent does not degrade up to a modulation frequency of 10 kHz; moreover, the photocurrent depends linearly on the incident power. These results indicate that the photogating effect observed previously in other nanomaterials[43,44] is not likely to play an important role here.

In addition to the 1.81° TBG, we also measured the photoresponse in a 1.15° TBG (the photoresponse and TCC are presented in Supplementary Section 3). We observed very similar photoresponse properties to those reported in Fig. 1c, as shown in Supplementary Fig. 3a. In fact, theoretical calculations predict the existence of the superlattice bandgap from 2° to ~1.05° (refs. [4,12,13]). As a result, it is not surprising that the photoresponse properties are similar in the 1.81° and 1.15° TBG devices. In the latter, photoresponse decrease at slightly high V_{DS} is also observed (see Supplementary Fig. 3b,c). Besides, the peak responsivities of the 1.81° TBG device are generally higher than those of the 1.15° TBG. Two factors could contribute to this observation. First, the superlattice-induced bandgap (at four electrons/holes per moiré) for the 1.81° TBG is larger than that of the 1.15° TBG[7], but they are still smaller than the lowest photon energy in our experiment, which is around 100 meV (12 μm light). As shown in Fig. 2a, the optical absorption is higher for photons with energies closer to the bandgap. Second, the conductance for the 1.81° TBG (Fig. 2b) when the Fermi level is inside the superlattice bandgap at 83 K is higher than that of the 1.15° TBG (Supplementary Fig. 4a). For a bolometer, as the photocurrent can be expressed as $I_{ph} = V_{DS} \times G \times TCC \times \Delta T$ (ref. [45], where ΔT is the effective carrier temperature change), the higher conductance in the 1.81° TBG can also lead to a larger photoresponse.

We also want to emphasize that we do not distinguish the difference between the electron and phonon temperatures in the photocurrent estimation above. In our devices, the electron and phonon temperatures can be different, due to a sizeable V_{DS}. The TCC presented in the inset of Fig. 2b was measured at a condition close to equilibrium (V_{DS} = 10 mV), where electrons and phonons have almost the same temperature. Nevertheless, the formula $I_{ph} = V_{DS} \times G \times TCC \times \Delta T$ still captures the physics of photocurrent generation. The positive TCC when the Fermi level is tuned within the superlattice gap is due to the carrier density dependence on electron temperature. In this case, the TBG is close to intrinsic and the enhanced electron temperature notably increases the free carrier density, leading to a positive TCC. Away from the superlattice gap, the TBG is doped and has a substantial amount of free charges. A higher electron temperature does not change the free carrier density considerably. In this case the scattering of free carrier dominates the TCC, which is negative due to the enhanced scattering at higher temperature.

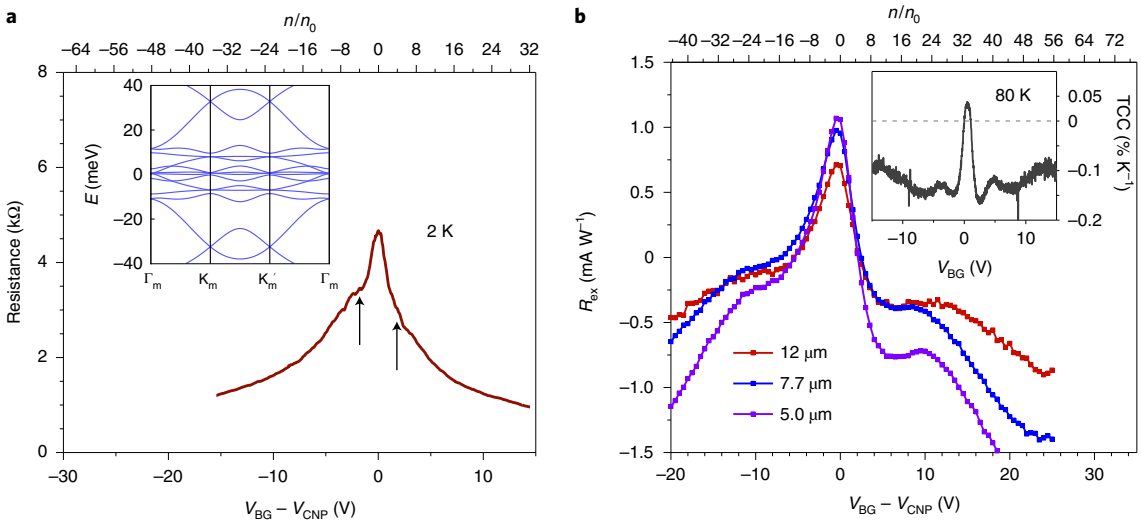

Fig. 3 | Photoresponse in bilayer graphene with ultrasmall twist angle. a, The resistance of the ultrasmall-twist-angle TBG device as a function of back-gate voltage at 2 K. There are two small side ripples next to the Dirac point peak, denoted by the black arrows. They correspond to electron filling states of ±4, from which the twist angle of 0.37° is obtained. The inset shows the calculated band structure of the 0.37° TBG. No superlattice bandgap is observed within the plotted energy range. **b**, The extrinsic photoresponsivity of the device under 5.0 μm, 7.7 μm and 12 μm light illuminations at 83 K. The photoresponse shows a small and positive peak at around the Dirac points, which is distinctively different from that in the TBG with a bandgap. The inset shows the TCC calculated from the temperature-dependent transport measurements.

Other than TBGs with a superlattice bandgap (with a twist angle from around 1° to 2°), it is also interesting to investigate the photoresponse in ultrasmall-twist-angle TBGs, in which previous theoretical and experimental transport characteristics do not indicate a superlattice bandgap opening[4,9]. The superlattice bandgaps at electron filling states of ±4 often close when the twist angle is slightly below 1° and hardly reopen as the twist angle further decreases[11]. We measured the gate-dependent photoresponse in a TBG with an ultrasmall twist angle of ~0.37°. As plotted in Fig. 3a, the source–drain resistance of such a small twist-angle device does not exhibit major side peaks in both the electron and hole branches, even at 2 K, which is distinctively different from the transport properties reported in TBGs with twist angles of 1.81° (Fig. 1b) and 1.15° (Supplementary Fig. 4a). We estimate the twist angle in this case by noticing two small side ripples, as denoted by the arrows. The two side ripples are positioned at ±1.80 V back-gate voltages (with carrier densities of $\pm 3.17 \times 10^{11}$ cm^{-2}) relative to the charge-neutrality point, corresponding to electron filling states of ±4 (ref. [9]), from which a twist angle of 0.37° is deduced as before. We emphasize that there is no insulating behaviour at these two ripple positions and superlattice bandgaps do not exist within the plotted electron filling range from $-32\,n_0$ to $32\,n_0$ (Supplementary Section 4). As our devices have a two-terminal configuration, contact resistance can smear the intrinsic transport features of the TBG channel. As a result, these ripples are not as evident as those reported previously[9], but are still visible. There is no superlattice bandgap from $-32\,n_0$ to $32\,n_0$ at such a small twist angle, as also evidenced by the calculated band structure in the inset of Fig. 3a. Note that this nature would not be changed by the complex lattice relaxation and reconstruction[9]. The gate-dependent photoresponse of this TBG is plotted in Fig. 3b. No photoresponse peak exists in the electron or hole branches. Moreover, at the Dirac points (the charge-neutrality point), we observe weak positive photoresponsivity of around 1.2 mA W^{-1} in this ultrasmall-twist-angle TBG. This observation is different from those in TBGs with relatively large twist angles where the responsivity does not reach a positive value at the Dirac points. This is probably due to the different band structures around the Dirac points when the twist angles are different. In fact, the measured TCC (see the inset of Fig. 3b) on this device also supports our measured positive photoresponse at the Dirac points. A small, positive TCC of 0.05% K^{-1} is observed.

As a comparison, we also fabricated AB-stacked bilayer graphene devices that were sandwiched between hBN layers and measured their mid-infrared photoresponse (see Supplementary Section 5 for the results). In short, due to the absence of a superlattice bandgap and the smaller DOS compared with that of TBG, the photoresponse is rather weak (<1.5 mA W^{-1}). It is also worth mentioning that dual-gate AB bilayer graphene bolometers have been demonstrated in a previous work by Yan and colleagues[46]. Their devices operate at 5 K and the voltage responsivity is as high as $\sim 2 \times 10^5$ V W^{-1}. Given the sample resistance of around 160 kΩ, the voltage responsivity can be converted into a current responsivity of around 1,250 mA W^{-1}. Such a responsivity is much greater than what is reported in our work; however, our devices operate at a higher temperature of around 80 K, at which the dual-gate AB bilayer graphene devices demonstrated by Yan et al. are no longer operational. In terms of physical mechanism, the bolometric effect is the dominant source of the photoresponse in both cases; however, our devices preserve the intrinsic properties of TBG by hBN encapsulation. Moreover, the DOS at the edges of superlattice bandgaps are enhanced due to the folding of the Brillouin zone, leading to increased absorption of mid-infrared light especially for 12 μm light. As a result, the hBN-encapsulated TBG represents a new platform for mid-infrared photonics, in addition to AB bilayer graphene.

Finally, we want to comment on the optimum twist angle for mid-infrared photodetection. For light with photon energies below ~100 meV, the optimum twist angle is probably the one for which the superlattice-induced gap approximately matches the photon energy, due to the strong absorption at the band edge (as suggested by the calculations in Fig. 2a). Despite the discrepancy between the calculated and measured superlattice bandgaps, it is expected to be less than ~100 meV (refs. [4,6,7,34,37,39]). As a result, for photon energies greater than 100 meV, there is no twist angle at which the bandgap matches the photon energy. In this case, the optimum choice is probably the twist angle that leads to the largest gaps. With a relatively large bandgap, the absorption can still be

probably enhanced for photon energies below ~200 meV. Moreover, the large bandgap can also lead to enhanced TCC when Fermi level is at the middle of the superlattice bandgap. As reported previously, the superlattice-induced bandgap first increases and then decreases from ~1° to 2° (refs. [4,34,37,39]). Beyond 2°, tuning the Fermi level to the middle of the bandgap is no longer feasible using regular dielectrics as the required doping is overwhelmingly large. According to the previous experimental results[34,37], the largest superlattice bandgap probably occurs when the twist angle is between 1.4° and 2°. In our experiments, we use three different lasers (12, 7.7 and 5.0 μm) and the photon energy is between 100 and 250 meV. As a result, the device performance should be optimal where the superlattice bandgap is the largest. In fact, we fabricated and measured around ten devices with various twist angles, finding that the 1.81° TBG device exhibits the best result (Supplementary Section 6). This observation is consistent with previous experimental works on the superlattice bandgaps of TBGs with different twist angles.

In summary, we report the strong mid-infrared photoresponse in TBGs with superlattice-induced bandgaps and superlattice-enhanced DOS. Such TBGs show strong photoresponse in a broad mid-infrared wavelength range from 5 to 12 μm, reaching an extrinsic peak responsivity of 26 mA W^{-1} at 12 μm. Moreover, we reveal that the twist angle plays a critical role and such strong photoresponse vanishes when twist angle is ultrasmall, due to the closing of the superlattice-induced bandgap. Our results demonstrate the promising role of TBGs in tunable mid-infrared optoelectronic applications.

Online content

Any methods, additional references, Nature Research reporting summaries, source data, extended data, supplementary information, acknowledgements, peer review information; details of author contributions and competing interests; and statements of data and code availability are available at https://doi.org/10.1038/s41566-020-0644-7.

Received: 5 November 2019; Accepted: 28 April 2020;
Published online: 01 June 2020

References

1. Lopes dos Santos, J. M. B., Peres, N. M. R. & Castro Neto, A. H. Graphene bilayer with a twist: electronic structure. *Phys. Rev. Lett.* **99**, 256802 (2007).
2. Mele, E. J. Commensuration and interlayer coherence in twisted bilayer graphene. *Phys. Rev. B* **81**, 161405 (2010).
3. Bistritzer, R. & MacDonald, A. H. Moiré bands in twisted double-layer graphene. *Proc. Natl Acad. Sci. USA* **108**, 12233–12237 (2011).
4. Cao, Y. et al. Superlattice-induced insulating states and valley-protected orbits in twisted bilayer graphene. *Phys. Rev. Lett.* **117**, 116804 (2016).
5. Kim, K. et al. Tunable moiré bands and strong correlations in small-twist-angle bilayer graphene. *Proc. Natl Acad. Sci. USA* **114**, 3364–3369 (2017).
6. Cao, Y. et al. Unconventional superconductivity in magic-angle graphene superlattices. *Nature* **556**, 43–50 (2018).
7. Cao, Y. et al. Correlated insulator behaviour at half-filling in magic-angle graphene superlattices. *Nature* **556**, 80–84 (2018).
8. Yankowitz, M. et al. Tuning superconductivity in twisted bilayer graphene. *Science* **363**, 1059–1064 (2019).
9. Yoo, H. et al. Atomic and electronic reconstruction at the van der Waals interface in twisted bilayer graphene. *Nat. Mater.* **18**, 448–453 (2019).
10. Sharpe, A. L. et al. Emergent ferromagnetism near three-quarters filling in twisted bilayer graphene. *Science* **365**, 605–608 (2019).
11. Codecido, E. et al. Correlated insulating and superconducting states in twisted bilayer graphene below the magic angle. *Sci. Adv.* **5**, eaaw9770 (2019).
12. Moon, P. & Koshino, M. Energy spectrum and quantum Hall effect in twisted bilayer graphene. *Phys. Rev. B* **85**, 195458 (2012).
13. Trambly de Laissardière, G., Mayou, D. & Magaud, L. Numerical studies of confined states in rotated bilayers of graphene. *Phys. Rev. B* **86**, 125413 (2012).
14. Ma, C. et al. Discovery of high dimensional band topology in twisted bilayer graphene. Preprint at https://arxiv.org/abs/1903.07950 (2019).
15. Wu, F., Lovorn, T., Tutuc, E., Martin, I. & MacDonald, A. H. Topological insulators in twisted transition metal dichalcogenide homobilayers. *Phys. Rev. Lett.* **122**, 086402 (2019).
16. Wang, Y., Wang, Z., Yao, W., Liu, G.-B. & Yu, H. Interlayer coupling in commensurate and incommensurate bilayer structures of transition-metal dichalcogenides. *Phys. Rev. B* **95**, 115429 (2017).
17. Lu, X. et al. Superconductors, orbital magnets and correlated states in magic-angle bilayer graphene. *Nature* **574**, 653–657 (2019).
18. Xu, S. G. et al. Giant oscillations in a triangular network of one-dimensional states in marginally twisted graphene. *Nat. Commun.* **10**, 4008 (2019).
19. Huang, S. et al. Topologically protected helical states in minimally twisted bilayer graphene. *Phys. Rev. Lett.* **121**, 037702 (2018).
20. Tabert, C. J. & Nicol, E. J. Optical conductivity of twisted bilayer graphene. *Phys. Rev. B* **87**, 121402 (2013).
21. Moon, P. & Koshino, M. Optical absorption in twisted bilayer graphene. *Phys. Rev. B* **87**, 205404 (2013).
22. Le, H. A. & Do, V. N. Electronic structure and optical properties of twisted bilayer graphene calculated via time evolution of states in real space. *Phys. Rev. B* **97**, 125136 (2018).
23. Li, G. et al. Observation of Van Hove singularities in twisted graphene layers. *Nat. Phys.* **6**, 109–113 (2009).
24. Kim, C.-J. et al. Chiral atomically thin films. *Nat. Nanotechnol.* **11**, 520–524 (2016).
25. Ponomarenko, L. A. et al. Cloning of Dirac fermions in graphene superlattices. *Nature* **497**, 594–597 (2013).
26. Dean, C. R. et al. Hofstadter's butterfly and the fractal quantum hall effect in moiré superlattices. *Nature* **497**, 598–602 (2013).
27. Hunt, B. et al. Massive Dirac fermions and Hofstadter butterfly in a van der Waals heterostructure. *Science* **340**, 1427–1430 (2013).
28. Patel, H. et al. Tunable optical excitations in twisted bilayer graphene form strongly bound excitons. *Nano Lett.* **15**, 5932–5937 (2015).
29. Yin, J. et al. Selectively enhanced photocurrent generation in twisted bilayer graphene with van Hove singularity. *Nat. Commun.* **7**, 10699 (2016).
30. Xin, W. et al. Photovoltage enhancement in twisted-bilayer graphene using surface plasmon resonance. *Adv. Opt. Mater.* **4**, 1703–1710 (2016).
31. Yu, K. et al. Gate tunable optical absorption and band structure of twisted bilayer graphene. *Phys. Rev. B* **99**, 241405 (2019).
32. Patel, H., Huang, L., Kim, C.-J., Park, J. & Graham, M. W. Stacking angle-tunable photoluminescence from interlayer exciton states in twisted bilayer graphene. *Nat. Commun.* **10**, 1445 (2019).
33. Kim, K. et al. Van der Waals heterostructures with high accuracy rotational alignment. *Nano Lett.* **16**, 1989–1995 (2016).
34. Chung, T.-F., Xu, Y. & Chen, Y. P. Transport measurements in twisted bilayer graphene: electron-phonon coupling and Landau level crossing. *Phys. Rev. B* **98**, 035425 (2018).
35. Levine, B. F., Gunapala, S. D., Kuo, J. M., Pei, S. S. & Hui, S. Normal incidence hole intersubband absorption long wavelength GaAs/$Al_xGa_{1-x}As$ quantum well infrared photodetectors. *Appl. Phys. Lett.* **59**, 1864–1866 (1991).
36. Gunapala, S. D. et al. Long-wavelength 640 × 486 GaAs/AlGaAs quantum well infrared photodetector snap-shot camera. *IEEE Trans. Electron Dev.* **45**, 1890–1895 (1998).
37. Polshyn, H. et al. Large linear-in-temperature resistivity in twisted bilayer graphene. *Nat. Phys.* **15**, 1011–1016 (2019).
38. Nair, R. R. et al. Fine structure constant defines visual transparency of graphene. *Science* **320**, 1308–1308 (2008).
39. Nam, N. N. T. & Koshino, M. Lattice relaxation and energy band modulation in twisted bilayer graphene. *Phys. Rev. B* **96**, 075311 (2017).
40. Liddiard, K. C. Thin-film resistance bolometer IR detectors. *Infrared Phys* **24**, 57–64 (1984).
41. Richards, P. L. Bolometers for infrared and millimeter waves. *J. Appl. Phys.* **76**, 1–24 (1994).
42. Chanin, G. & Torre, J. P. Electrothermal model for ideal semiconductor bolometers. *J. Opt. Soc. Am. A* **1**, 412–419 (1984).
43. Guo, Q. et al. Black phosphorus mid-infrared photodetectors with high gain. *Nano Lett.* **16**, 4648–4655 (2016).
44. Furchi, M. M., Polyushkin, D. K., Pospischil, A. & Mueller, T. Mechanisms of photoconductivity in atomically thin MoS_2. *Nano Lett.* **14**, 6165–6170 (2014).
45. Guo, Q. et al. Efficient electrical detection of mid-infrared graphene plasmons at room temperature. *Nat. Mater.* **17**, 986–992 (2018).
46. Yan, J. et al. Dual-gated bilayer graphene hot-electron bolometer. *Nat. Nanotechnol.* **7**, 472–478 (2012).

Methods

Fabrication of TBG transistors. The fabrication of the device started with mechanical exfoliation of monolayer graphene and hBN flakes on SiO_2-covered silicon substrates; hBNs with thicknesses of ~30 nm were typically chosen. The hBN/TBG/hBN stack was assembled and transferred onto 90 nm-thick SiO_2 on a silicon substrate, using the previously reported polypropylene carbonate-assisted 'tear and stack' dry transfer method[4,33]. The stack was then annealed at 600 °C for 6 h. Clean areas free of bubbles and residues were then identified for device fabrication. The device channel was defined using a Vistec 100 kV electron-beam lithography system, followed by sulfur hexafluoride plasma dry etch. Chromium/gold (4/40 nm) metal contacts were deposited onto the two ends of the channel to form edge contacts[47].

Low-temperature transport measurements. The electrical transport measurements down to 83 K were performed in a modified Linkam HFS600E-PB4 cryostat. An Agilent B1500A semiconductor parameter analyser was used to apply gate voltages, source–drain bias and measure the resistance. We used a small V_{DS} of 10 mV during the transport measurements to minimize V_{DS}-induced doping non-uniformity across the devices. The electrical transport measurements down to 2 K were performed in the Quantum Design physical property measurement system DynaCool. A Stanford Research SR830 lock-in amplifier was used to apply an alternating I_{DS} of 100 nA at 17.777 Hz while simultaneously monitoring the in-phase V_{DS}. A Keithley 2400 source meter was used to apply the gate voltages.

Photocurrent measurements and responsivity calculations. The infrared light (5.0 μm, 7.7 μm or 12 μm) emitted from a quantum cascade laser was coupled to a Bruker Vertex 70 Fourier-transform infrared spectrometer and focused on the sample using a Hyperion 2000 infrared microscope. The sample was placed in the modified Linkam HFS600E-PB4 cryostat, which was mounted on the Fourier-transform infrared spectrometer stage. The cryostat was filled with argon and then cooled to 83 K. The light was chopped at 917 Hz by a mechanical chopper. The source–drain bias was applied using a Keithley 2612 source meter and the photocurrent was collected by means of a Stanford Research SR830 lock-in amplifier in series with a Femto DLPCA-200 current amplifier. The back-gate voltage was applied by the same source meter. A LabVIEW program swept the gate voltage while recording the photocurrent and device resistance.

The responsivity calculations mainly involved the calibrations of incident light power on a device. The light power under the infrared microscope was measured by a Thorlabs S401C thermal power sensor. The powers were 350 μW, 1,200 μW and 1,100 μW for the 5.0 μm, 7.7 μm and 12 μm laser light used in the experiments, respectively. As our devices (3 μm × 3 μm) are smaller than the beam spot, we need to calibrate the incident power on a device. We calibrated the beam spot size and position using the knife-edge technique, assuming a Gaussian beam shape. For the 5.0 μm laser spot on sample chip, the standard deviations were measured to be $\sigma_x = 6.0$ μm and $\sigma_y = 9.0$ μm along two perpendicular directions. As a result, by positioning device in the middle of the beam spot, the incident power on the device was calculated to be 9.1 μW. For the 7.7 μm and 12 μm incident light, the same method was applied and the light powers on device were 13 μW and 5.3 μW, respectively. We finally calculated the responsivity using the directly measured photocurrent divided by the power on device.

Theoretical model for moiré band structures. We obtain the moiré band structures of TBG with small twist angles by using the 2011 Bistritzer–MacDonald model[3]. In this model, the AA and AB tunnelling amplitudes are $t_{AA} = t_{AB} = 110$ meV, the Fermi velocity is $v_F = 1 \times 10^6$ m s^{-1}, and the flat bands appear at the first magic angle 1.08°. Koshino et al. suggested[48] using $t_{AA} = 79.7$ meV, $t_{AB} = 97.5$ meV and $v_F = 7.98 \times 10^5$ m s^{-1} to accommodate the effect of lattice relaxation. In this work, we use these updated parameters. The momentum cutoff used in these calculations is six times as large as the moiré reciprocal lattice vectors. The considered area in the momentum space, which is centred at the K point of the original Brillouin zone, is 108 times as large as the area of the first mini-Brillouin zone. To obtain the optical transitions, we discretized the first mini-Brillouin zone into a mesh with 120,000 points (with the hexagonal symmetry intact) and used 1 meV as the integrated energy interval. Each moiré band is spin degenerate, as the spin-orbit coupling is negligibly weak in TBG. The moiré bands at valley K′ of the original Brillouin zone (not shown) can be readily obtained by leveraging the time-reversal symmetry from the bands at valley K. As evidenced by many graphene experiments, the two valleys are well decoupled in the bulk yet unavoidably coupled near atomic edges.

Optical absorption calculations. During an optical transition event, the momentum is conserved for the initial state $|i\rangle$ and the final state $|f\rangle$; we ignore the photon momentum. As a result, only direct transitions between bands are taken into account in our calculations and the calculation processes are similar to those reported in ref. [38]. The incident energy flux is $W_i = \frac{c}{4\pi}|\boldsymbol{\Theta}|^2$ and the absorbed energy per unit time is $W_a = \eta\hbar\omega$. Here $\boldsymbol{\Theta}$ and ω are the electric field and frequency of the light, respectively, and the absorption events per unit time (η) can be calculated by using Fermi's Golden rule as $\eta = \left(\frac{2\pi}{\hbar}\right)|M|^2 D$, where $M = \langle f|H_{int}|i\rangle$ is the matrix element for the Hamiltonian of the light–electron interaction H_{int}, and D is the joint DOS at the photon frequency. The light–electron interaction can be obtained by the Hamiltonian $H = v_F\boldsymbol{\sigma}\cdot\left(\mathbf{p} - \frac{e}{c}\mathbf{A}\right) = H_0 + H_{int}$, which is the same for both graphene layers in the small-twist-angle limit. Here e is the elementary charge, $\mathbf{p}$ is the momentum, $\mathbf{A} = \frac{ic}{\omega}\boldsymbol{\Theta}$ is the vector potential and $\boldsymbol{\sigma}$ represents the Pauli matrices of the two sublattices. H_0 is the low-energy Hamiltonian for monolayer graphene and $H_{int} = v_F\boldsymbol{\sigma}\cdot\frac{e}{i\omega}\boldsymbol{\Theta}$ is the light–electron interaction. The absorption can be expressed by $P = \frac{\langle W_a\rangle}{W_i}$. The interaction matrix element, $\langle f|\boldsymbol{\sigma}\cdot\boldsymbol{\Theta}|i\rangle$, and D need to be calculated numerically. Note that for monolayer graphene, $P = \frac{\pi e^2}{\hbar c}$.

Data availability

The data that support the plots within this paper and other findings of this study are available from the corresponding authors on reasonable request.

References

47. Wang, L. et al. One-dimensional electrical contact to a two-dimensional material. *Science* **342**, 614–617 (2013).
48. Koshino, M. et al. Maximally localized Wannier orbitals and the extended Hubbard model for twisted bilayer graphene. *Phys. Rev. X* **8**, 031087 (2018).

Acknowledgements

We acknowledge financial support from the National Science Foundation EFRI-NewLAW programme (grant no. 1741693). We also thank the Office of Naval Research for partial support in the experimental set-ups. The theoretical work at UTD is supported by the Army Research Office under grant no. W911NF-18-1-0416 and the Natural Science Foundation under grant no. DMR-1921581 through the DMREF programme. Growth of hexagonal boron nitride crystals was supported by the Elemental Strategy Initiative conducted by the MEXT, Japan and the CREST (grant no. JPMJCR15F3), JST. We also acknowledge L. Wang, D. Hynek, J. Woods, J. Cha at Yale West Campus and our previous group member X. Chen for their support.

Author contributions

B.D., C.M. and S.Y. fabricated and characterized the devices. Q.W. and F.Z. performed the theoretical calculations. K.W. and T.T. synthesized the hBN crystals. F.X., F.Z., B.D. and Q.W. drafted the manuscript. All the authors discussed the results and commented on the manuscript.

Competing interests

The authors declare no competing interests.

Additional information

Supplementary information is available for this paper at https://doi.org/10.1038/s41566-020-0644-7.

Correspondence and requests for materials should be addressed to F.Z. or F.X.

Reprints and permissions information is available at www.nature.com/reprints.